



# NiFe (Oxy) Hydroxides Derived from NiFe Disulfides as an Efficient Oxygen Evolution Catalyst for Rechargeable Zn–Air Batteries: The Effect of Surface S Residues

Tanyuan Wang, Gyutae Nam, Yue Jin, Xingyu Wang, Pengju Ren, Min Gyu Kim, Jiashun Liang, Xiaodong Wen, Haeseong Jang, Jiantao Han, Yunhui Huang, Qing Li,\* and Jaephil Cho\*

A facile  $\text{H}_2\text{O}_2$  oxidation treatment to tune the properties of metal disulfides for oxygen evolution reaction (OER) activity enhancement is introduced. With this method, the degree of oxidation can be readily controlled and the effect of surface S residues in the resulted metal (oxy)hydroxides for the OER is revealed for the first time. The developed NiFe (oxy)hydroxide catalyst with residual S demonstrates an extraordinarily low OER overpotential of 190 mV at the current density of  $10 \text{ mA cm}^{-2}$  after coupling with carbon nanotubes, and outstanding performance in Zn–air battery tests. Theoretical calculation suggests that the surface S residues can significantly reduce the adsorption free energy difference between  $\text{O}^{\bullet\bullet}$  and  $\text{OH}^{\bullet\bullet}$  intermediates on the Fe sites, which should account for the high OER activity of NiFe (oxy)hydroxide catalysts. This work provides significant insight regarding the effect of surface heteroatom residues in OER electrocatalysis and offers a new strategy to design high-performance and cost-efficient OER catalysts.

Oxygen evolution reaction (OER) is considered as one of the most important reactions in sustainable energy conversion and storage technology.<sup>[1–3]</sup> It is involved in some of the mostly studied clean energy conversion systems including water splitting,  $\text{CO}_2$  reduction, and rechargeable metal–air batteries.<sup>[4–7]</sup> Especially, Zn–air batteries suffer from degradation of air

electrode during charging process due to the high charging overpotential.<sup>[8,9]</sup> In this regard, the sluggish kinetics of OER requires efficient catalysts to reduce the overpotential. Precious metal oxides such as  $\text{IrO}_2$  and  $\text{RuO}_2$  are well-known OER electrocatalysts with high activity but suffer from high cost and low abundance. Hence considerable efforts have been devoted to developing cost-effective OER catalysts derived from earth-abundance elements. First-row transition metal (mainly Fe, Co, Ni, Mn) compounds including oxides,<sup>[10,11]</sup> (oxy)hydroxides,<sup>[12,13]</sup> phosphates,<sup>[14]</sup> phosphides,<sup>[15–17]</sup> sulfides,<sup>[18]</sup> selenides,<sup>[19,20]</sup> and nitrides<sup>[21]</sup> are the mostly studied nonprecious metal OER catalysts. Among these compounds, the metal oxides and (oxy)hydroxides display some of the most outstanding OER performance.<sup>[22–24]</sup> In addition, recent studies reveal that the essential active sites of the metal phosphides, sulfides, and selenides for OER are likely the surface oxides/(oxy)hydroxides species formed during the electrochemical oxidation process.<sup>[25,26]</sup> With this in mind, the synthetic and structural tuning of metal oxides/(oxy)hydroxides toward

Dr. T. Wang, J. Liang, Prof. J. Han, Prof. Y. Huang, Prof. Q. Li

State Key Laboratory of Material Processing and Die & Mould Technology

School of Materials Science and Engineering  
Huazhong University of Science and Technology  
Wuhan 430074, China

E-mail: qing\_li@hust.edu.cn

Dr. G. Nam, H. Jang, Prof. J. Cho

Department of Energy Engineering and School of Energy and Chemical Engineering

Ulsan National Institute of Science and Technology (UNIST)  
Ulsan 44919, South Korea

E-mail: jpcho@unist.ac.kr

Dr. Y. Jin

Institute of Apicultural Research  
Chinese Academy of Agricultural Science  
Beijing 100093, China

X. Wang

College of Chemistry and Molecular Engineering

Peking University

Beijing 100871, China

X. Wang, P. Ren, Prof. X. Wen

State Key Laboratory of Coal Conversion

Institute of Coal Chemistry

Chinese Academy of Sciences

P.O. Box 165, Taiyuan, Shanxi 030001, P. R. China & Synfuels China

Beijing 100195, China

Dr. M. G. Kim

Beamline Research Division

Pohang Accelerator Laboratory

Pohang University of Science and Technology

Pohang 790-784, South Korea

The ORCID identification number(s) for the author(s) of this article can be found under <https://doi.org/10.1002/adma.201800757>.

DOI: 10.1002/adma.201800757

enhanced activity and stability has been a focus in OER electrocatalysis. Numerous methods have been proposed to improve the OER activity of the metal oxides/(oxy)hydroxides, including fabricating ultrathin or 3D structures,<sup>[27–29]</sup> synthesizing multimetal oxides/(oxy)hydroxides,<sup>[12,13,30,31]</sup> and ameliorating the conductivity of the materials by using conductive supports.<sup>[10,32,33]</sup>

Recently, *in situ* electrochemical oxidation of metal chalcogenides (S and Se) is reported as a new strategy to fabricate metal oxides as promising OER catalysts.<sup>[24,26]</sup> Noteworthy, in these cases the chalcogenides are believed to be completely converted to oxides and the enhanced OER activity compared to common metal oxides are ascribed to the increased electrochemical surface areas/porosities/defects and reduced grain sizes during the electrochemical oxidation process. However, the nature of the active sites and the mechanism of OER catalysis enhancement have yet to be fully understood. For Fe containing multimetal (Ni, Co, etc.) oxides/(oxy)hydroxides, OH\* intermediate prefers absorbing on FeOOH sites due to their strong affinity<sup>[34]</sup> but too strong absorption of OH\* on Fe sites would possibly compromise their OER performance.<sup>[35]</sup> In principle, the partly substitution of O by S may reduce the valence state of Fe and optimize the absorption energy of intermediates, thus tuning OER activity of the catalysts. In this study, the critical role of surface S residues in metal (oxy)hydroxides derived from metal sulfides in OER performance enhancement is reported for the

first time. S-incorporated NiFe (oxy)hydroxides are developed by a facile and controllable chemical oxidation of NiFe disulfides and the effect of residual S in NiFe (oxy)hydroxides on OER catalysis is systematically studied. The optimized NiFe (oxy) hydroxide demonstrates extraordinarily high OER activity in 1.0 M KOH with the overpotential as low as 190 mV at 10 mA cm<sup>-2</sup> when supported on carbon nanotubes (CNTs). In rechargeable Zn-air battery tests, the developed catalyst shows less overpotential in charge process and much improved durability relative to the-state-of-the-art Pt/C-IrO<sub>2</sub> electrode. Theoretical calculation suggests that the surface S residues can optimize the adsorption free energy of the OER intermediates on Fe sites (which are proved to be the OER active site for NiFe (oxy)hydroxide<sup>[34]</sup>) and significantly reduce the adsorption energy gap between O\* and OH\*.<sup>[22]</sup>

The Ni<sub>x</sub>Fe<sub>1-x</sub>—OH ( $x = 1, 6/7, 3/4$ ) catalysts were fabricated by a two-step method derived from metal sulfides (Figure 1a, for details see the **Experimental Section** in the Supporting Information). By controlling the oxidation degree of the sulfides precursor, the NiFe (oxy)hydroxides with different amounts of S residues can be prepared. The final catalysts are denoted as Ni<sub>x</sub>Fe<sub>1-x</sub>—OH-2, Ni<sub>x</sub>Fe<sub>1-x</sub>—OH-6, and Ni<sub>x</sub>Fe<sub>1-x</sub>—OH-24 with oxidation times of 2, 6, and 24 h, respectively. As shown in Figure 1a, Ni<sub>6/7</sub>Fe<sub>1/7</sub>S<sub>2</sub> sample demonstrates nanorod morphology with diameters of 200–300 nm. The morphology of the Ni<sub>6/7</sub>Fe<sub>1/7</sub>S<sub>2</sub> changes obviously from nanorods to nanoflakes after being

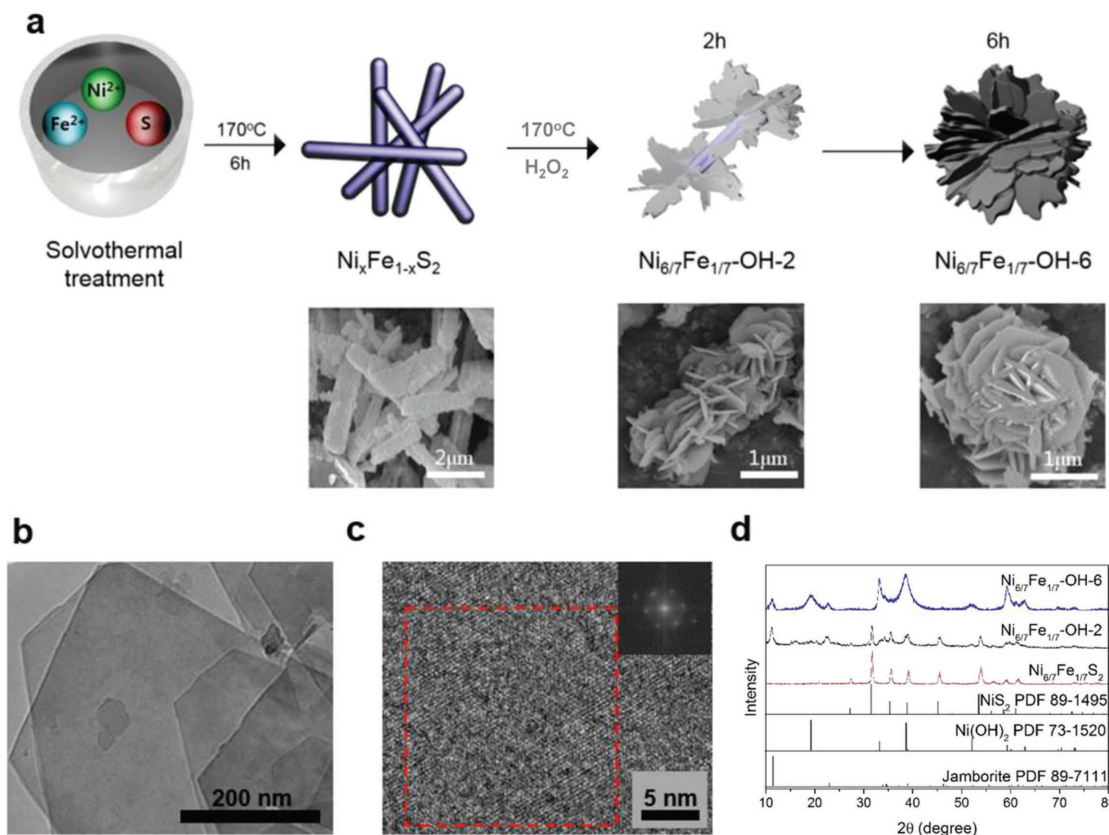


**Figure 1.** a) Schematic illustration and SEM images of the preparation of the Ni<sub>6/7</sub>Fe<sub>1/7</sub>S<sub>2</sub>, Ni<sub>6/7</sub>Fe<sub>1/7</sub>—OH-2, and Ni<sub>6/7</sub>Fe<sub>1/7</sub>—OH-6 catalysts. b) TEM, and c) HRTEM images of the Ni<sub>6/7</sub>Fe<sub>1/7</sub>—OH-6 catalyst, the inset in (c) is an FFT image of the red frame region. d) XRD patterns of the Ni<sub>6/7</sub>Fe<sub>1/7</sub>S<sub>2</sub>, Ni<sub>6/7</sub>Fe<sub>1/7</sub>—OH-2, and Ni<sub>6/7</sub>Fe<sub>1/7</sub>—OH-6 samples.

treated with  $H_2O_2$  for 2 h, which reveals that the surface of NiFe sulfide has been converted to NiFe (oxy)hydroxide. After reacting for 6 h, all the  $Ni_{6/7}Fe_{1/7}S_2$  nanorods have turned into flower-like  $Ni_xFe_{1-x}-OH$  structures. When the oxidation time increases to 24 h, the sample transforms to large nanosheets with diameters of several micrometers (Figure S1, Supporting Information), indicating a nearly complete oxidative conversion to layered NiFe hydroxides. The elemental composition of all studied samples measured by energy dispersive X-ray spectroscopy (EDX) is listed in Table S1 in the Supporting Information and the atomic S contents in  $Ni_{6/7}Fe_{1/7}S_2$ ,  $Ni_{6/7}Fe_{1/7}-OH-2$ ,  $Ni_{6/7}Fe_{1/7}-OH-6$ , and  $Ni_{6/7}Fe_{1/7}-OH-24$  are 48.67%, 31.59%, 2.41%, and 0.24%, respectively.

The transmission electron microscopic (TEM) image of the  $Ni_{6/7}Fe_{1/7}-OH-6$  sample (Figure 1b) reveals nanoflake morphology with sizes of several hundred nanometers. High-resolution TEM (HRTEM) image (Figure 1c) indicates the crystalline nature in the  $Ni_{6/7}Fe_{1/7}-OH-6$  nanosheets and the fast Fourier transform (FFT) image (Figure 1c inset) suggests a lattice spacing of 0.26 nm. The well-crystallized domain can be more easily observed in high-angle annular dark field-scanning transmission electron microscopic image (Figure S2a, Supporting Information). The lattice fringes with interplanar distance of  $\approx 0.26$  nm can be corresponded to the (012) planes of jamborite ( $NiOOH/Ni(OH)_2$  hybrid). Figure 1d displays the X-ray diffraction (XRD) patterns of  $Ni_{6/7}Fe_{1/7}S_2$ ,  $Ni_{6/7}Fe_{1/7}-OH-2$ , and  $Ni_{6/7}Fe_{1/7}-OH-6$  samples. The  $Ni_{6/7}Fe_{1/7}S_2$  sample shows a typical crystal structure of cubic  $NiS_2$  (JCPDF No. 89-1495). After reacting with  $H_2O_2$  for 2 h,  $Ni_{6/7}Fe_{1/7}S_2$  is partially oxidized and converted to a mixed phase of  $NiS_2$  and jamborite (hybrid of  $\beta-Ni(OH)_2$  and  $\gamma-NiOOH$ , JCPDF No. 89-7111). Importantly,  $Ni_{6/7}Fe_{1/7}-OH-6$  appears to be transformed to a mixed phase of hexagonal  $\beta-Ni(OH)_2$  (JCPDF No. 73-1520) and jamborite.  $Ni_{6/7}Fe_{1/7}-OH-24$  shows similar XRD pattern (Figure S3, Supporting Information) compared with  $Ni_{6/7}Fe_{1/7}-OH-6$  but the peaks of sulfide disappear. It is of note that previously reported metal oxides obtained by the in situ electrochemical oxidation of sulfides usually exhibit very poor crystalline or amorphous structure.<sup>[24,36]</sup> In the contrast, our NiFe (oxy)hydroxides synthesized via chemical oxidation are well-crystallized, which may benefit the conductivity and structural stability of the catalysts.

Since the low electron-conductivity nature of NiFe (oxy) hydroxides limits its OER performance,<sup>[31,37]</sup> multiwall CNTs are employed as catalyst supports to improve the conductivity of the catalysts. Figures S2b and S4 in the Supporting Information present the scanning electron microscopy (SEM) and TEM images of the  $Ni_{6/7}Fe_{1/7}-OH-6/CNT$  composite catalyst. The CNTs wrap on the surface of  $Ni_{6/7}Fe_{1/7}-OH$  flowers and connect with separated nanosheets, thereby enhancing the conductivity of the catalyst. EDX elemental mapping images of Ni, Fe, O, and S elements in Figure S2c in the Supporting Information indicate that all four elements are uniformly distributed on the nanosheets, even though the S signal is less prominent relative to other three elements. The mole ratio of S to (S + O) is about 3:100 according to the EDX characterization (Figure S5, Supporting Information), which indicates that there is still  $\approx 3\%$  S that have not been oxidized in  $Ni_{6/7}Fe_{1/7}-OH-6/CNT$  catalyst.

X-ray photoelectron spectroscopy (XPS) is employed to characterize the surface electronic states of the developed catalysts.

Figure S6 in the Supporting Information displays the survey spectra of  $Ni_{6/7}Fe_{1/7}S_2$  and  $Ni_{6/7}Fe_{1/7}-OH$  samples with different oxidation times. The S signals of the samples after oxidation treatment is extremely weak regardless of oxidation time. Figure 2a shows the high resolution Ni 2p spectrum of  $Ni_{6/7}Fe_{1/7}S_2$ . A pair of peaks with Ni 2p<sub>3/2</sub> peak at 853.4 eV can be assigned to Ni(II) that fully binds with S. After being oxidized for 6 h, this pair of Ni 2p peaks vanishes and two new pairs of peaks appear (Figure 2d). The Ni 2p<sub>3/2</sub> peak at 855.1 eV represents lower valence Ni that bind with O or S, while the Ni 2p<sub>3/2</sub> peak at 857.0 eV should be related to NiOOH.<sup>[26]</sup> Noteworthy that even though the dominant crystal phase in  $Ni_{6/7}Fe_{1/7}-OH-6$  should be  $Ni(OH)_2$ , as measured in XRD, the surface of the sample is Ni(III)-rich. The Ni 2p profiles of  $Ni_{6/7}Fe_{1/7}-OH-2$  (Figure S7, Supporting Information) and  $Ni_{6/7}Fe_{1/7}-OH-24$  (Figure 2g) are similar to that of  $Ni_{6/7}Fe_{1/7}-OH-6$ , but their relative intensities of Ni(III) peaks are a little weaker. On the other hand, high resolution S 2p spectrum of  $Ni_{6/7}Fe_{1/7}S_2$  (Figure 2b) shows a pair of peaks at 162.2 and 163.4 eV, corresponding to the sulfide structure. After oxidation treatment, trace amount of S could still be observed in S 2p XPS spectra of  $Ni_{6/7}Fe_{1/7}-OH-2$  (Figure S8, Supporting Information) and  $Ni_{6/7}Fe_{1/7}-OH-6$  (Figure 2e) samples with a positively shifted binding energy (S 2p<sub>3/2</sub> peak at 165.8 eV), but disappears in that of  $Ni_{6/7}Fe_{1/7}-OH-24$  (Figure 2h). This result manifests that residual S does exist on the surface of  $Ni_{6/7}Fe_{1/7}-OH-2$  and  $Ni_{6/7}Fe_{1/7}-OH-6$  ( $\approx 1$  at%) samples. Note-worthy, the vertical S distribution of  $Ni_{6/7}Fe_{1/7}-OH-6$  should not be homogeneous as the S at surface is much less than that in bulk. Figure 2c,f,i, and Figure S9 (Supporting Information) show the Fe 2p spectra of  $Ni_{6/7}Fe_{1/7}S_2$  and  $Ni_{6/7}Fe_{1/7}-OH$  catalysts. It is found that Fe mainly exists as Fe(II) on the surface of  $Ni_{6/7}Fe_{1/7}S_2$ . After the  $H_2O_2$  treatment, the surface Fe of all samples was converted to Fe(III) regardless of oxidation time. However, the binding energies of Fe 2p<sub>3/2</sub> peaks for  $Ni_{6/7}Fe_{1/7}-OH-2$  and  $Ni_{6/7}Fe_{1/7}-OH-6$  samples are slightly lower than that of  $Ni_{6/7}Fe_{1/7}-OH-24$ . Possible explanation is that after 24 h oxidation treatment, S are nearly completely removed and Fe are all bonded with O on the surface and thus lead to the increased binding energy of Fe.

The OER performance of the catalysts was measured in 1.0 M KOH by linear sweep voltammetry (LSV). Figure 3a displays the OER activity of  $Ni_xFe_{1-x}S_2$  and  $Ni_xFe_{1-x}-OH-6$  catalysts with different elemental compositions. The  $Ni_{6/7}Fe_{1/7}S_2$  catalyst demonstrates an onset potential of 1.5 V versus reversible hydrogen electrode (RHE) and an overpotential of 350 mV at the current density of 10 mA cm<sup>-2</sup>. After being treated with  $H_2O_2$  for 6 h, the OER activity of the obtained  $Ni_{6/7}Fe_{1/7}-OH-6$  catalyst improves significantly. Its onset potential is only 1.4 V versus RHE with an overpotential of 270 mV to reach the current density of 10 mA cm<sup>-2</sup>, much lower than that of the commercial  $IrO_2$  (340 mV at 10 mA cm<sup>-2</sup>). Tafel slopes of the studied catalysts also decrease from 69 mV dec<sup>-1</sup> ( $Ni_{6/7}Fe_{1/7}S_2$ ) to 40 mV dec<sup>-1</sup> ( $Ni_{6/7}Fe_{1/7}-OH-6$ ) after oxidation (Figure 3b), further confirming the benefit of the  $H_2O_2$  treatment for the OER activity enhancement.  $NiS_2$  (Figure S10a, Supporting Information) and  $Ni_{3/4}Fe_{1/4}S_2$  (Figure S10b, Supporting Information) samples with nanorod structures are also synthesized and oxidized for 6 h to obtain  $Ni-OH-6$  (Figure S10c, Supporting Information)

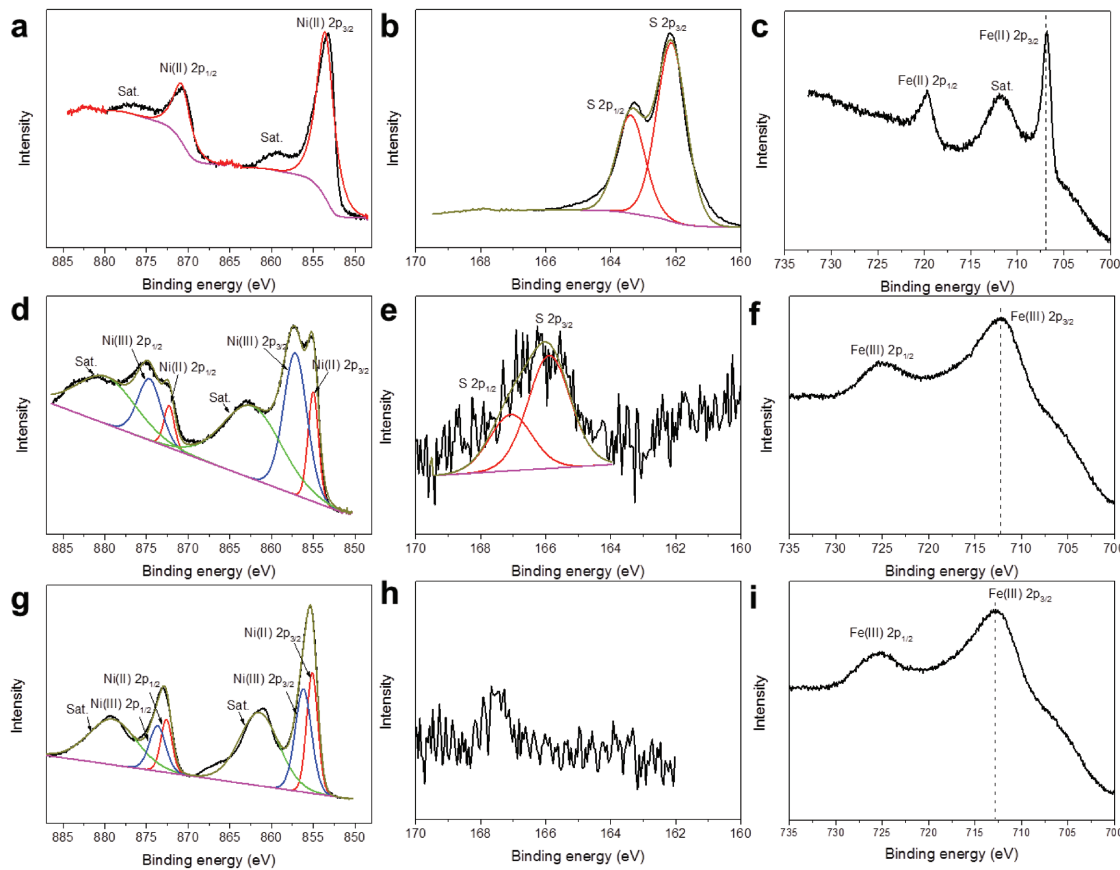


**Figure 2.** High resolution Ni 2p XPS spectra for: a)  $\text{Ni}_{6/7}\text{Fe}_{1/7}\text{S}_2$ , d)  $\text{Ni}_{6/7}\text{Fe}_{1/7}-\text{OH-6}$ , and g)  $\text{Ni}_{6/7}\text{Fe}_{1/7}-\text{OH-24}$  samples. High resolution S 2p XPS spectra for: b)  $\text{Ni}_{6/7}\text{Fe}_{1/7}\text{S}_2$ , e)  $\text{Ni}_{6/7}\text{Fe}_{1/7}-\text{OH-6}$ , and h)  $\text{Ni}_{6/7}\text{Fe}_{1/7}-\text{OH-24}$  samples. High resolution Fe 2p XPS spectra for: c)  $\text{Ni}_{6/7}\text{Fe}_{1/7}\text{S}_2$ , f)  $\text{Ni}_{6/7}\text{Fe}_{1/7}-\text{OH-6}$ , and i)  $\text{Ni}_{6/7}\text{Fe}_{1/7}-\text{OH-24}$  samples.

and  $\text{Ni}_{3/4}\text{Fe}_{1/4}-\text{OH-6}$  (Figure S10d, Supporting Information) catalysts. Both of them exhibit sheet-like structures which are similar to that of the  $\text{Ni}_{6/7}\text{Fe}_{1/7}-\text{OH-6}$  sample. Ni–OH-6 displays quite low OER activity with a large Tafel slope, suggesting the key role of Fe in boosting the OER activity. It is worth noting that higher Fe/Ni ratio would lead to worse OER performance. The overpotential required to achieve  $10 \text{ mA cm}^{-2}$  measured on  $\text{Ni}_{3/4}\text{Fe}_{1/4}-\text{OH-6}$  is 330 mV, which is inferior to that of  $\text{Ni}_{6/7}\text{Fe}_{1/7}-\text{OH-6}$  catalyst. Figure S11 in the Supporting Information shows the cyclic voltammetry (CV) curves of Ni–OH-6,  $\text{Ni}_{3/4}\text{Fe}_{1/4}-\text{OH-6}$ ,  $\text{Ni}_{6/7}\text{Fe}_{1/7}-\text{OH-6}$ , and  $\text{Ni}_{6/7}\text{Fe}_{1/7}\text{S}_2$  samples in 1.0 M KOH.  $\text{Ni}_{6/7}\text{Fe}_{1/7}-\text{OH-6}$  demonstrates an increased electrochemical double layer capacitive current compared with  $\text{Ni}_{6/7}\text{Fe}_{1/7}\text{S}_2$  (calculated capacitance: 5.2 vs  $1.3 \text{ mF cm}^{-2}$ ), indicating enhanced electrochemical surface area compared to that of  $\text{Ni}_{6/7}\text{Fe}_{1/7}\text{S}_2$ . Importantly, the capacitive currents of Ni–OH-6,  $\text{Ni}_{3/4}\text{Fe}_{1/4}-\text{OH-6}$ , and  $\text{Ni}_{6/7}\text{Fe}_{1/7}-\text{OH-6}$  are essentially similar, which suggest comparable electrochemical surface areas for these samples. As a result, it can be deduced that the catalyst morphology and surface area play an insignificant role in determining their OER activity.

To demonstrate the effect of  $\text{H}_2\text{O}_2$  treatment,  $\text{Ni}_{6/7}\text{Fe}_{1/7}\text{S}_2$  was also treated at 170 °C for 6 h in the absence of  $\text{H}_2\text{O}_2$ . No obvious change in morphology could be observed for the resulted  $\text{Ni}_{6/7}\text{Fe}_{1/7}\text{S}_2$  (Figure S12, Supporting Information) and

its OER activity is much lower than that of  $\text{Ni}_{6/7}\text{Fe}_{1/7}-\text{OH-6}$  (Figure S13, Supporting Information), which reveals the importance of  $\text{H}_2\text{O}_2$  oxidation in promoting the OER activity of metal sulfides. The influence of oxidation time on the OER performance of the  $\text{Ni}_{6/7}\text{Fe}_{1/7}-\text{OH}$  catalysts is also investigated (Figure 3c). Overall, all the oxidized samples show improvements in onset potential for OER relative to untreated one. Among all the studied catalysts,  $\text{Ni}_{6/7}\text{Fe}_{1/7}-\text{OH-2}$  and  $\text{Ni}_{6/7}\text{Fe}_{1/7}-\text{OH-6}$  demonstrate significantly superior activity to other ones and  $\text{Ni}_{6/7}\text{Fe}_{1/7}-\text{OH-6}$  performs best. The OER activity of  $\text{Ni}_{6/7}\text{Fe}_{1/7}-\text{OH-24}$  is not as high as the one with shorter oxidation time, suggesting the insufficient activity of fully oxidized NiFe hydroxides. According to Table S1 in the Supporting Information and XPS results, the amount of residual S decreases with the extension of oxidation time. Considering the similar bulk structures of  $\text{Ni}_{6/7}\text{Fe}_{1/7}-\text{OH-6}$  and  $\text{Ni}_{6/7}\text{Fe}_{1/7}-\text{OH-24}$  catalysts, as reflected in XRD, it is assumed that the surface S residues may play a significant role in promoting the OER activity of NiFe (oxy)hydroxide catalysts. On the other hand, XPS characterizations reveal that the surface Ni(III) concentration of  $\text{Ni}_{6/7}\text{Fe}_{1/7}-\text{OH-6}$  is slightly higher than that of  $\text{Ni}_{6/7}\text{Fe}_{1/7}-\text{OH-2}$  (Figure 2; Figure S7, Supporting Information), which likely accounts for the better OER activity of the  $\text{Ni}_{6/7}\text{Fe}_{1/7}-\text{OH-6}$  catalyst than  $\text{Ni}_{6/7}\text{Fe}_{1/7}-\text{OH-2}$  as Ni(III) species are more OER active than Ni(II).

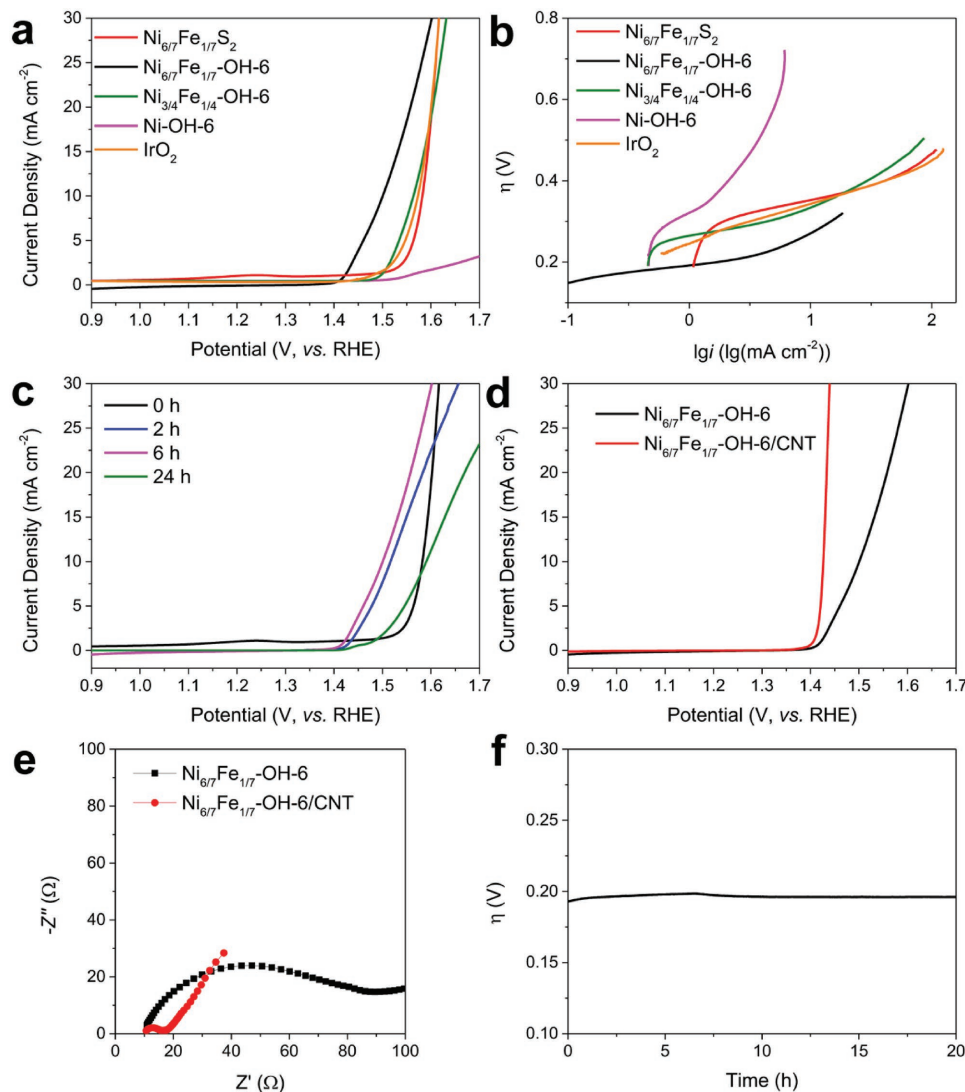


**Figure 3.** a) LSV curves of  $\text{IrO}_2$ ,  $\text{Ni}_{6/7}\text{Fe}_{1/7}\text{S}_2$ , and S-incorporated  $\text{Ni}_{x}\text{Fe}_{1-x}-\text{OH}$  with different Ni/Fe ratios in 1.0 M KOH at a scan rate of 10 mV s<sup>-1</sup>. b) Tafel slopes of  $\text{IrO}_2$ ,  $\text{Ni}_{6/7}\text{Fe}_{1/7}\text{S}_2$  and S-incorporated  $\text{Ni}_{x}\text{Fe}_{1-x}-\text{OH}$  with different Ni/Fe ratios toward OER. c) LSV curves of the  $\text{Ni}_{6/7}\text{Fe}_{1/7}-\text{OH}$  catalysts with different oxidation times. d) LSV curves of  $\text{Ni}_{6/7}\text{Fe}_{1/7}-\text{OH-6}$  and  $\text{Ni}_{6/7}\text{Fe}_{1/7}-\text{OH-6/CNT}$  hybrid catalysts in 1.0 M KOH at a scan rate of 10 mV s<sup>-1</sup>. e) Nyquist plots of  $\text{Ni}_{6/7}\text{Fe}_{1/7}-\text{OH-6}$  and  $\text{Ni}_{6/7}\text{Fe}_{1/7}-\text{OH-6/CNT}$  hybrid catalysts at an overpotential of 210 mV. f) Stability test of the  $\text{Ni}_{6/7}\text{Fe}_{1/7}-\text{OH-6/CNT}$  hybrid at a current density of 10 mA cm<sup>-2</sup>.

CNTs are employed as conducting supports to further boost the OER activity of the  $\text{Ni}_{6/7}\text{Fe}_{1/7}-\text{OH-6}$  catalyst. Figure 3d reveals the OER performance of  $\text{Ni}_{6/7}\text{Fe}_{1/7}-\text{OH-6}$  before and after the addition of CNTs. Obviously, the  $\text{Ni}_{6/7}\text{Fe}_{1/7}-\text{OH-6/CNT}$  hybrid shows significant improvement in OER activity compared to that of standalone  $\text{Ni}_{6/7}\text{Fe}_{1/7}-\text{OH-6}$ . The Tafel slope of the  $\text{Ni}_{6/7}\text{Fe}_{1/7}-\text{OH-6/CNT}$  catalyst decreases notably at high overpotential region and reaches as low as 24 mV dec<sup>-1</sup> (Figure S14, Supporting Information). Electrochemical impedance spectroscopy was further employed to evaluate the charge transfer process of electrode reactions.  $\text{Ni}_{6/7}\text{Fe}_{1/7}-\text{OH-6}$  without CNT displays a charge transfer resistance of about 80  $\Omega$  at the overpotential of 210 mV, while the charge transfer resistance of hybrid catalyst is only about 10  $\Omega$  for OER (Figure 3e), attesting to the significant enhancement in electron-conductivity. Importantly, the developed  $\text{Ni}_{6/7}\text{Fe}_{1/7}-\text{OH-6/CNT}$

catalyst can achieve the current density of 10 mA cm<sup>-2</sup> at a low overpotential of 190 mV, which is among the best OER electrocatalysts reported so far (Table S2, Supporting Information). The  $\text{Ni}_{6/7}\text{Fe}_{1/7}-\text{OH-6/CNT}$  hybrid also demonstrates excellent OER durability. Its overpotential ( $\eta$ ) keeps stable even after continuous electrolysis at a current density of 10 mA cm<sup>-2</sup> for 20 h (Figure 3f). XPS characterization proves that the residual S still remains in the sample after stability (Figure S15, Supporting Information), which demonstrates the decent structural stability of the  $\text{Ni}_{6/7}\text{Fe}_{1/7}-\text{OH-6/CNT}$  catalyst.

To gain further insight into the origin of extraordinarily high OER activity of the developed NiFe (oxy)hydroxide catalysts derived from  $\text{H}_2\text{O}_2$  oxidation of NiFe sulfides, the OER activity–structure correlation of a series of metal oxides/hydroxides ( $\text{Fe}-\text{OH}$ ,  $\text{Co}-\text{OH}$ ,  $\text{Ni}-\text{OH}$ ,  $\text{Ni}_{6/7}\text{Fe}_{1/7}-\text{OH}$ ) that prepared by the direct precipitation of metal ions followed by  $\text{H}_2\text{O}_2$

oxidation for 6 h were systematically studied. Both Ni–OH and  $\text{Ni}_{6/7}\text{Fe}_{1/7}$ –OH show sheet-like structure while Fe–OH and Co–OH consist of much smaller nanoparticles (Figure S16, Supporting Information). From CV curves (Figure S17, Supporting Information), Co–OH exhibits the largest capacitance current while Fe–OH displays the smallest one. The OER performance of these samples is displayed in Figure S18 in the Supporting Information. All the metal oxides/hydroxides show improved OER activity after treatment except Fe–OH. It may be due to that  $\text{H}_2\text{O}_2$  oxidation induces the formation of OER active  $\text{CoOOH}$  and  $\text{NiOOH}$  sites, while  $\text{FeOOH}$  is not as active as Co and Ni counterparts for OER. It is of note that the OER activity of the  $\text{Ni}_{6/7}\text{Fe}_{1/7}$ –OH after  $\text{H}_2\text{O}_2$  oxidation is lower than  $\text{Ni}_{6/7}\text{Fe}_{1/7}$ –OH-6 derived from sulfide. Based on the comprehensive structural characterizations shown above, we can conclude that the surface S residues in the NiFe (oxy)hydroxides should be the main factor contributing to their extremely high OER activity.

A rechargeable Zn–air battery (Figure S19, Supporting Information) was constructed with the best-performing  $\text{Ni}_{6/7}\text{Fe}_{1/7}$ –OH-6/CNT as the cathode catalyst due to its excellent OER performance and acceptable catalytic activity for ORR (Figure S20, Supporting Information). **Figure 4a** and Figure S21 (Supporting Information) display the polarization

curves of  $\text{Ni}_{6/7}\text{Fe}_{1/7}$ –OH-6/CNT and the mixture of Pt/C and  $\text{IrO}_2$  by increasing (dis)charge current densities until potential difference reaches 2.2 V (over 2.5 V for charge process and under 0.3 V for discharge process to prohibit degradation of the air electrode). The mixture of Pt/C and  $\text{IrO}_2$  exhibits higher discharge working potential than  $\text{Ni}_{6/7}\text{Fe}_{1/7}$ –OH-6/CNT until  $300 \text{ mA cm}^{-2}$ , but in the charge process,  $\text{Ni}_{6/7}\text{Fe}_{1/7}$ –OH-6/CNT performs less overpotential than the mixture of Pt/C and  $\text{IrO}_2$ . In addition, we performed rechargeable Zn–air battery test with two different conditions. In low depth of (dis)charge condition (10 min for 1 cycle, 1%),  $\text{Ni}_{6/7}\text{Fe}_{1/7}$ –OH-6/CNT presents stable potential difference ( $\approx 0.55 \text{ V}$ ) from the 1st cycle to the 150th cycle while the mixture of Pt/C and  $\text{IrO}_2$  performs increasing overpotential ( $\approx 0.5 \text{ V}$ ) during cycling (Figure 4b). At the 150th cycle,  $\text{Ni}_{6/7}\text{Fe}_{1/7}$ –OH-6/CNT reveals significantly better durability than the mixture of Pt/C and  $\text{IrO}_2$  due to its excellent OER performance (Figure 4c). Under another high depth of (dis)charge condition (4 h for 1 cycle, 20%), the overall tendency exhibits similar to low depth of (dis)charge condition (Figure 4d). Especially, the voltage difference of  $\text{Ni}_{6/7}\text{Fe}_{1/7}$ –OH-6/CNT decreases along with increased cycle number while the mixture of Pt/C and  $\text{IrO}_2$  performs increased overpotential, which signifies potential application of the developed catalyst in the rechargeable Zn–air battery.

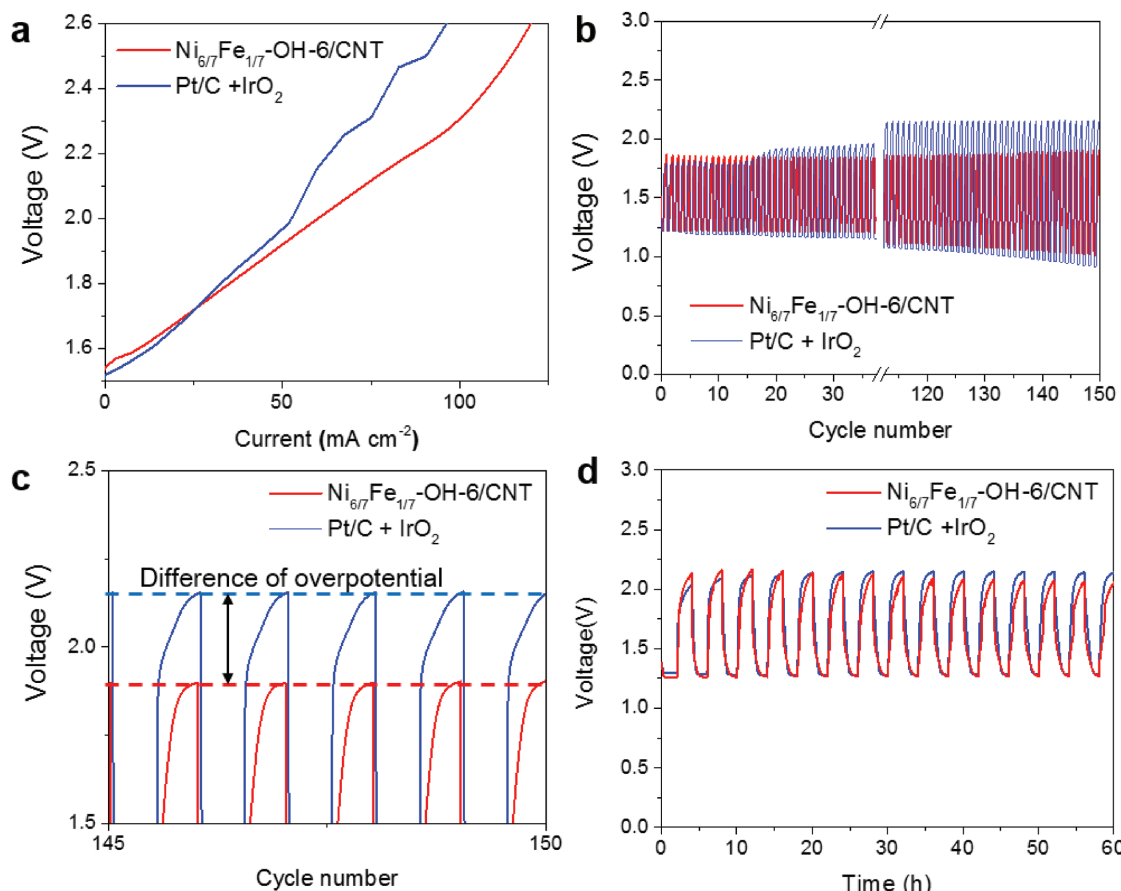


**Figure 4.** a) The current-voltage profiles of the rechargeable Zn–air batteries of the  $\text{Ni}_{6/7}\text{Fe}_{1/7}$ –OH-6/CNT catalyst and the mixture of Pt/C and  $\text{IrO}_2$ . b) The rechargeable Zn–air battery cycling profiles with  $15 \text{ mA cm}^{-2}$  of (dis)charge current density. c) The magnified cycle images of inset (b) (OER charge process region from the 145th cycle to 150th cycle). d) The rechargeable Zn–air battery cycling profiles with  $20 \text{ mA cm}^{-2}$  of (dis)charge current density.

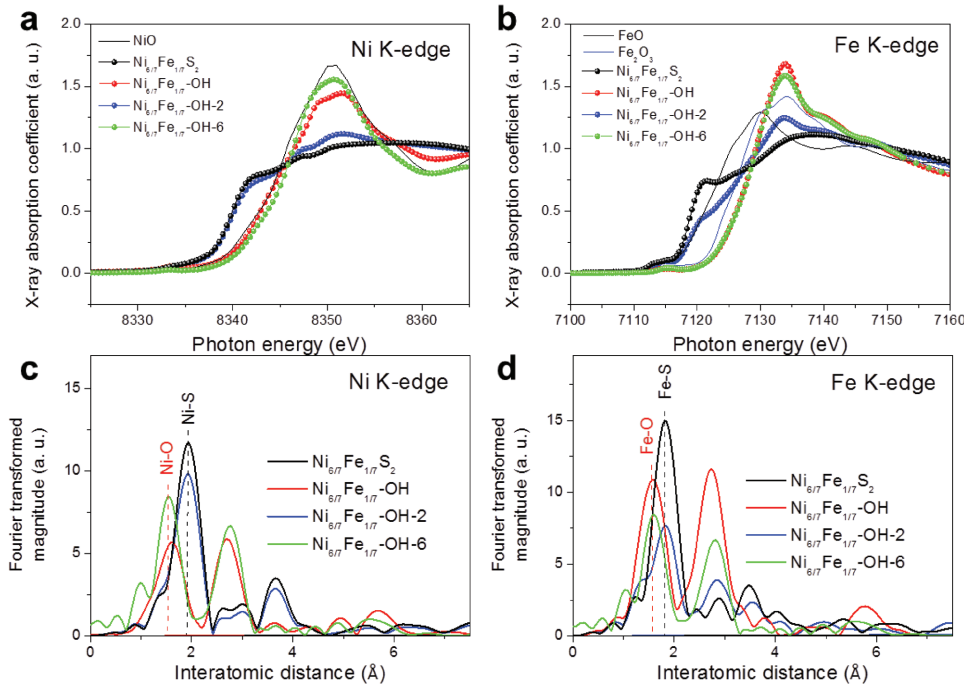


**Figure 5.** a,b) Normalized Ni (a), and Fe (b) K-edge XANES spectra for Ni<sub>6/7</sub>Fe<sub>1/7</sub>S<sub>2</sub>, Ni<sub>6/7</sub>Fe<sub>1/7</sub>-OH (without residual S), Ni<sub>6/7</sub>Fe<sub>1/7</sub>-OH-2, and Ni<sub>6/7</sub>Fe<sub>1/7</sub>-OH-6. c,d) Radial distribution functions of Ni (c), Fe (d) K-edge  $k^3$ -weighted EXAFS spectra for Ni<sub>6/7</sub>Fe<sub>1/7</sub>S<sub>2</sub>, Ni<sub>6/7</sub>Fe<sub>1/7</sub>-OH (no residual S), Ni<sub>6/7</sub>Fe<sub>1/7</sub>-OH-2, and Ni<sub>6/7</sub>Fe<sub>1/7</sub>-OH-6.

The bulk structures of the developed catalysts were characterized by X-ray absorption spectroscopy. Figure 5a shows the Ni K-edge X-ray absorption near edge structure (XANES) spectra of Ni<sub>6/7</sub>Fe<sub>1/7</sub>-OH that are oxidized for 2 and 6 h. Ni<sub>6/7</sub>Fe<sub>1/7</sub>-OH-2 exhibits similar charge state with Ni<sub>6/7</sub>Fe<sub>1/7</sub>S<sub>2</sub>. Near 8353 eV, Ni<sub>6/7</sub>Fe<sub>1/7</sub>-OH-2 sample shows increased peak compared to that of Ni<sub>6/7</sub>Fe<sub>1/7</sub>S<sub>2</sub>, pointing to the existence of Ni–O bonding. On the other hand, Ni<sub>6/7</sub>Fe<sub>1/7</sub>-OH-6 demonstrates similar spectra to as-synthesized Ni<sub>6/7</sub>Fe<sub>1/7</sub>-OH and NiO samples, which suggests that Ni mainly exists as Ni(II) in the bulk. This result is consistent with XRD (Figure 1d) and implies that Ni(III) species formed by H<sub>2</sub>O<sub>2</sub> treatment are mainly present at the surface of the catalysts. Radial distribution functions of Ni K-edge  $k^3$ -weighted extended X-ray absorption fine structure (EXAFS) spectra depicted in Figure 5c suggest that Ni<sub>6/7</sub>Fe<sub>1/7</sub>-OH-2 contains both Ni–O and Ni–S bonds. However, due to the low bulk concentration of residual S (less than 5%), the Ni–S bond in Ni<sub>6/7</sub>Fe<sub>1/7</sub>-OH-6 is hard to be distinguished. The tendency in Fe K-edge XANES and EXAFS spectra of the Ni<sub>6/7</sub>Fe<sub>1/7</sub>-OH samples (Figure 5b,d) are similar to that in the Ni K-edge spectra. Overall, Ni<sub>6/7</sub>Fe<sub>1/7</sub>-OH-2 reveals both Fe–O and Fe–S bonds while Ni<sub>6/7</sub>Fe<sub>1/7</sub>-OH-6 contains mainly Fe–O bond with dominant Fe(III). However, the Ni–O bond length of Ni<sub>6/7</sub>Fe<sub>1/7</sub>-OH-6 is slightly shorter than that of Ni<sub>6/7</sub>Fe<sub>1/7</sub>-OH without residual S, while the Fe–O bond length of Ni<sub>6/7</sub>Fe<sub>1/7</sub>-OH-6 is slightly longer than that of Ni<sub>6/7</sub>Fe<sub>1/7</sub>-OH. The obvious surface Ni(III) signal of Ni<sub>6/7</sub>Fe<sub>1/7</sub>-OH-6 (Figure 2d) should contribute to the decreased Ni–O bond length since Ni in the bulk structure are mainly Ni<sup>2+</sup>, while the residual S may lead to the increased Fe–O bond length as S is less electronegative than O.

Density functional theory (DFT) calculations were employed to provide further insights into the role of the residual S toward the OER enhancement. According to XPS and XRD, the surface of Ni<sub>6/7</sub>Fe<sub>1/7</sub>-OH-6 should be rich in Ni<sub>x</sub>Fe<sub>1-x</sub>OOH. As reported in previous work, the surface substitution of Fe into NiOOH will enhance the OER activity.<sup>[35]</sup> Thus we design Fe-on-top structures as a comparison and set a similar surface termination to identify the effect of residual S (Figure 6; Figures S22–S24, Supporting Information). Single S atom is incorporated into the adjacency of both Ni and Fe. The models with S atom replacing O atom at the surface and in the subsurface of Ni<sub>x</sub>Fe<sub>1-x</sub>OOH (Figure 6a) are denoted as Ni<sub>x</sub>Fe<sub>1-x</sub>OOH–S-1 (Figure 6b) and Ni<sub>x</sub>Fe<sub>1-x</sub>OOH–S-2 (Figure 6c), respectively. The reaction mechanism and adsorption structures of all intermediates are illustrated in Figure 6d. The higher affinity of O-based adsorbates on Fe than on Ni leads to the more stabilization of intermediates on the top site of Fe atoms. Furthermore, the stability of all intermediates is moderately tuned after S was incorporated into the Ni<sub>x</sub>Fe<sub>1-x</sub>OOH. For O\*, the decreasing of free energy indicates it is stabilized by residual S, whereas for OH\*, its free energy is dependent on the doping configuration. Previous theoretical works indicate that the OER overpotential is directly linked with the free energies of the reaction intermediates (especially O\* and OH\*), and the adsorption free energy difference between O\* and OH\* is suggested to be the main descriptor for the OER activity of Fe, Co, and Ni-based oxides. The Ni<sub>x</sub>Fe<sub>1-x</sub>OOH–S-1 model (S incorporated at the surface) shows decreased OH\* adsorption free energy and the free energy gap between O\* and OH\* compared with the bare Ni<sub>x</sub>Fe<sub>1-x</sub>OOH, which implies lower OER overpotential for this model. Moreover, the Ni<sub>x</sub>Fe<sub>1-x</sub>OOH–S-2

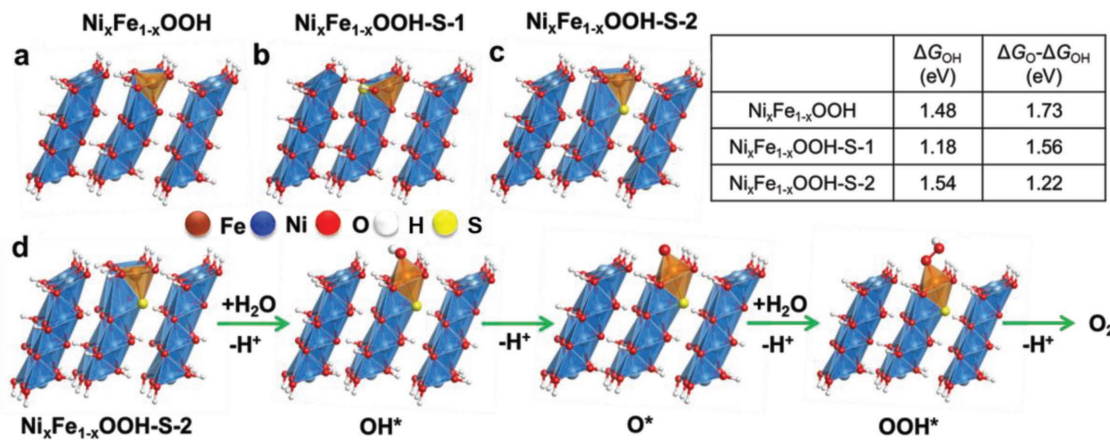


**Figure 6.** Theoretical calculation of the free energies for: a)  $\text{Ni}_x\text{Fe}_{1-x}\text{OOH}$  without residual S, b)  $\text{Ni}_x\text{Fe}_{1-x}\text{OOH-S-1}$  (S incorporated on the surface), and c)  $\text{Ni}_x\text{Fe}_{1-x}\text{OOH-S-2}$  (S incorporated in the subsurface) during OER. d) Reaction mechanism and structures of intermediates involved in OER for S-incorporated  $\text{Ni}_x\text{Fe}_{1-x}\text{OOH}$ .

model (S incorporated in the subsurface of the materials) shows a  $\text{O}^*$  to  $\text{OH}^*$  adsorption free energy difference of only 1.22 eV and  $\text{OH}^*$  adsorption free energy of 1.54 eV, which not only means high OER activity for the S-incorporated Fe sites but also reveals that  $\text{O}^*$  to  $\text{OH}^*$  free energy difference of the NiFe (oxy)hydroxides can be optimized by the residual S significantly. Specifically, the formation of  $\text{OH}^*$  turns to the rate-determining step for OER in this structure rather than the formation of  $\text{O}^*$ . By analyzing the electronic structure, it is also found that the change of  $\text{O}^*$  stability is correlated with the valence state of Fe. After S incorporation, the valence state of Fe is slightly reduced, as the Bader charge decrease from 1.70 to 1.61, which is due to that S possess less electronegativity than O. This may enhance the bonding between Fe and  $\text{O}^*$  and lead to lower OER overpotential.

In summary, we report S-incorporated NiFe (oxy)hydroxides derived from metal sulfides by a controllable chemical oxidation process as highly efficient OER catalysts for Zn-air batteries. The residual S at the catalyst surface is demonstrated to be vital to the OER activity of the developed NiFe (oxy)hydroxides and can be precisely tuned to maximize their OER performance. After compositing with CNTs, the best-performing  $\text{Ni}_{6/7}\text{Fe}_{1/7}-\text{OH-6}/\text{CNT}$  catalyst demonstrates an extremely low overpotential of 190 mV to achieve the current density of  $10 \text{ mA cm}^{-2}$  and a small Tafel slope of  $24 \text{ mV dec}^{-1}$ . In Zn-air battery test,  $\text{Ni}_{6/7}\text{Fe}_{1/7}-\text{OH-6}/\text{CNT}$  catalyst reveal better durability than the mixture of Pt/C and  $\text{IrO}_2$  electrode after 150 cycles. DFT calculation reveals that the surface S residues would significantly reduce the adsorption free energy gap between  $\text{O}^*$  and  $\text{OH}^*$  on Fe sites, thereby reducing the OER overpotential of the catalyst. This work offers a new concept to enhance the OER activity of the NiFe (oxy)hydroxides via tuning surface heteroatom residues and can be extended to other transition metal catalyst systems, which would hold potential promise for use in water splitting devices and rechargeable metal-air batteries.

## Supporting Information

Supporting Information is available from the Wiley Online Library or from the author.

## Acknowledgements

T.W. and G.N. contributed equally to this work. This work was financially supported by National 1000 Young Talents Program of China, National Nature Science Foundation of China (21603078, 21705052), National Materials Genome Project (2016YFB0700600), and China Postdoctoral Science Foundation (2017M610470, 2016M590216). Also, Research Fund (1.180036.01) of Ulsan National Institute of Science and Technology (UNIST) is greatly acknowledged. The authors thank the Analytical and Testing Center of Huazhong University of Science and Technology for carrying out the XPS and XRD measurements.

## Conflict of Interest

The authors declare no conflict of interest.

## Keywords

energy storage, NiFe hydroxides, oxygen evolution reaction, residual S, Zn-air batteries

Received: February 2, 2018

Revised: March 16, 2018

Published online:

- [1] Y. Jiao, Y. Zheng, M. T. Jaroniec, S. Z. Qiao, *Chem. Soc. Rev.* **2015**, 44, 2060.
- [2] I. Katsounaros, S. Cherevko, A. R. Zeradjanin, K. J. J. Mayrhofer, *Angew. Chem., Int. Ed.* **2014**, 53, 102.
- [3] Z. L. Wang, D. Xu, J. J. Xu, X. B. Zhang, *Chem. Soc. Rev.* **2014**, 43, 7746.
- [4] F. Y. Cheng, J. Chen, *Chem. Soc. Rev.* **2012**, 41, 2172.
- [5] M. G. Walter, E. L. Warren, J. R. McKone, S. W. Boettcher, Q. X. Mi, E. A. Santori, N. S. Lewis, *Chem. Rev.* **2010**, 110, 6446.
- [6] H. B. Gray, *Nat. Chem.* **2009**, 1, 7.
- [7] S. J. A. Moniz, S. A. Shevlin, D. J. Martin, Z. X. Guo, J. W. Tang, *Energy Environ. Sci.* **2015**, 8, 731.
- [8] J.-I. Jung, M. Risch, S. Park, M. G. Kim, G. Nam, H.-Y. Jeong, Y. Shao-Horn, J. Cho, *Energy Environ. Sci.* **2016**, 9, 176.

- [9] Y. G. Li, M. Gong, Y. Y. Liang, J. Feng, J.-E. Kim, H. L. Wang, G. S. Hong, B. Zhang, H. J. Dai, *Nat. Commun.* **2013**, *4*, 1805.
- [10] M. Gong, Y. G. Li, H. L. Wang, Y. Y. Liang, J. Z. Wu, J. G. Zhou, J. Wang, T. Regier, F. Wei, H. J. Dai, *J. Am. Chem. Soc.* **2013**, *135*, 8452.
- [11] L. Xu, Q. Q. Jiang, Z. H. Xiao, X. Y. Li, J. Huo, S. Y. Wang, L. M. Dai, *Angew. Chem., Int. Ed.* **2016**, *55*, 5277.
- [12] L. Trotochaud, S. L. Young, J. K. Ranney, S. W. Boettcher, *J. Am. Chem. Soc.* **2014**, *136*, 6744.
- [13] H. Y. Wang, Y. Y. Hsu, R. Chen, T. S. Chan, H. M. Chen, B. Liu, *Adv. Energy Mater.* **2015**, *5*, 1500091.
- [14] Y. Surendranath, M. W. Kanan, D. G. Nocera, *J. Am. Chem. Soc.* **2010**, *132*, 16501.
- [15] A. Mendoza-Garcia, H. Y. Zhu, Y. S. Yu, Q. Li, L. Zhou, D. Su, M. J. Kramer, S. H. Sun, *Angew. Chem., Int. Ed.* **2015**, *54*, 9642.
- [16] L. A. Stern, L. G. Feng, F. Song, X. L. Hu, *Energy Environ. Sci.* **2015**, *8*, 2347.
- [17] T. Y. Wang, C. Wang, Y. Jin, A. Sviripa, J. S. Liang, J. T. Han, Y. H. Huang, Q. Li, G. Wu, *J. Mater. Chem. A* **2017**, *5*, 25378.
- [18] W. J. Zhou, X. J. Wu, X. H. Cao, X. Huang, C. L. Tan, J. Tian, H. Liu, J. Y. Wang, H. Zhang, *Energy Environ. Sci.* **2013**, *6*, 2921.
- [19] C. Tang, N. Y. Cheng, Z. H. Pu, W. Xing, X. P. Sun, *Angew. Chem., Int. Ed.* **2015**, *54*, 9351.
- [20] Y. W. Liu, H. Cheng, M. J. Lyu, S. J. Fan, Q. H. Liu, W. S. Zhang, Y. D. Zhi, C. M. Wang, C. Xiao, S. Q. Wei, B. J. Ye, Y. Xie, *J. Am. Chem. Soc.* **2014**, *136*, 15670.
- [21] P. Z. Chen, K. Xu, Z. W. Fang, Y. Tong, J. C. Wu, X. L. Lu, X. Peng, H. Ding, C. Z. Wu, Y. Xie, *Angew. Chem., Int. Ed.* **2015**, *54*, 14710.
- [22] W. P. Sun, X. H. Rui, D. Zhang, Y. Z. Jiang, Z. Q. Sun, H. K. Liu, S. X. Dou, *J. Power Sources* **2016**, *309*, 135.
- [23] C. G. Morales-Guio, L. Liardet, X. L. Hu, *J. Am. Chem. Soc.* **2016**, *138*, 8946.
- [24] W. Chen, H. T. Wang, Y. Z. Li, Y. Y. Liu, J. Sun, S. H. Lee, J. S. Lee, Y. Cui, *ACS Cent. Sci.* **2015**, *1*, 244.
- [25] J. Ryu, N. Jung, J. H. Jang, H. J. Kim, S. J. Yoo, *ACS Catal.* **2015**, *5*, 4066.
- [26] X. Xu, F. Song, X. L. Hu, *Nat. Commun.* **2016**, *7*, 12324.
- [27] S. Chen, J. J. Duan, P. J. Bian, Y. H. Tang, R. K. Zheng, S. Z. Qiao, *Adv. Energy Mater.* **2015**, *5*, 1500936.
- [28] K. Fominykh, J. M. Feckl, J. Sicklinger, M. Doblinger, S. Bocklein, J. Ziegler, L. Peter, J. Rathousky, E. W. Scheidt, T. Bein, D. Fattakhova-Rohlfing, *Adv. Funct. Mater.* **2014**, *24*, 3123.
- [29] J. F. Ping, Y. X. Wang, Q. P. Lu, B. Chen, J. Z. Chen, Y. Huang, Q. L. Ma, C. L. Tan, J. Yang, X. H. Cao, Z. J. Wang, J. Wu, Y. B. Ying, H. Zhang, *Adv. Mater.* **2016**, *28*, 7640.
- [30] M. W. Louie, A. T. Bell, *J. Am. Chem. Soc.* **2013**, *135*, 12329.
- [31] M. Gong, H. J. Dai, *Nano Res.* **2015**, *8*, 23.
- [32] Y. Hou, Z. H. Wen, S. M. Cui, X. L. Feng, J. H. Chen, *Nano Lett.* **2016**, *16*, 2268.
- [33] S. Chen, J. J. Duan, M. Jaroniec, S. Z. Qiao, *Angew. Chem., Int. Ed.* **2013**, *52*, 13567.
- [34] D. Friebel, M. W. Louie, M. Bajdich, K. E. Sanwald, Y. Cai, A. M. Wise, M. J. Cheng, D. Sokaras, T. C. Weng, R. Alonso-Mori, R. C. Davis, J. R. Bargar, J. K. Norskov, A. Nilsson, A. T. Bell, *J. Am. Chem. Soc.* **2015**, *137*, 1305.
- [35] B. Zhang, X. L. Zheng, O. Voznyy, R. Comin, M. Bajdich, M. Garcia-Melchor, L. L. Han, J. X. Xu, M. Liu, L. R. Zheng, F. P. G. de Arquer, C. T. Dinh, F. J. Fan, M. J. Yuan, E. Yassitepe, N. Chen, T. Regier, P. F. Liu, Y. H. Li, P. De Luna, A. Janmohamed, H. L. L. Xin, H. G. Yang, A. Vojvodic, E. H. Sargent, *Science* **2016**, *352*, 333.
- [36] W. Chen, Y. Y. Liu, Y. Z. Li, J. Sun, Y. C. Qiu, C. Liu, G. M. Zhou, Y. Cui, *Nano Lett.* **2016**, *16*, 7588.
- [37] M. Zhou, Q. H. Weng, X. Y. Zhang, X. Wang, Y. M. Xue, X. H. Zeng, Y. Bando, D. Golberg, *J. Mater. Chem. A* **2017**, *5*, 4335.